THE 22nd CHESAPEAKE SAILING YACHT SYMPOSIUM

ANNAPOLIS, MARYLAND, MARCH 2016

Modal Analysis of Pressures on a Full-Scale Spinnaker

Julien Deparday[1], Naval Academy Research Institute, Brest, France
Patrick Bot, Naval Academy Research Institute, Brest, France
Fréderic Hauville, Naval Academy Research Institute, Brest, France
Benoit Augier, Naval Academy Research Institute, Brest, France
Marc Rabaud, Laboratoire FAST, Univ.Paris-Sud, CNRS, Université Paris-Saclay, F-91405, Orsay, France
Dario Motta, University of Auckland, New-Zealand
David Le Pelley, University of Auckland, New-Zealand

NOTATION

AWA	Apparent Wind Angle
AWS	Apparent Wind Speed
IQR	Inter Quartile Range (Q3-Q1)
Q1	First Quartile
Q3	Third Quartile
POD	Proper Orthogonal Decomposition
C_F	Load Coefficient ($\frac{\text{Load}}{\frac{1}{2}\rho\,\text{S}(\text{AWS})^2}$)
ΔC_P	Differential pressure coefficient ($\frac{P_{leeward}-P_{windward}}{\frac{1}{2}\rho(\text{AWS})^2}$)
ρ	Density of air (1.25 kg/m^3)
S	Sail Area of the asymmetrical Spinnaker (65 m^2)

ABSTRACT

While sailing offwind, the trimmer typically adjusts the downwind sail "on the verge of luffing", letting occasionally the luff of the sail flapping. Due to the unsteadiness of the spinnaker itself, maintaining the luff on the verge of luffing needs continual adjustments. The propulsive force generated by the offwind sail depends on this trimming and is highly fluctuating. During a flapping sequence, the aerodynamic load can fluctuate by 50% of the average load.

On a J/80 class yacht, we simultaneously measured time-resolved pressures on the spinnaker, aerodynamic loads, boat and wind data. Significant spatio-temporal patterns are detected in the pressure distribution. In this paper we present averages and main fluctuations of pressure distributions and of load coefficients for different apparent wind angles as well as a refined analysis of pressure fluctuations, using the Proper Orthogonal Decomposition (POD) method.

POD shows that pressure fluctuations due to luffing of the spinnaker can be well represented by only one proper mode related to a unique spatial pressure pattern and a dynamic behavior evolving with the Apparent Wind Angles. The time evolution of this proper mode is highly correlated with load fluctuations.

Moreover, POD can be employed to filter the measured pressures more efficiently than basic filters. The reconstruction using the first few modes allows to restrict to the most energetic part of the signal and remove insignificant variations and noises. This might be helpful for comparison with other measurements and numerical simulations.

INTRODUCTION

In research and development in sail aerodynamics, full-scale testing, wind tunnel testing and numerical simulation have always been complementary. Numerical simulation allows to efficiently investigate different designs without the cost of creating sails (Chapin *et al.*, 2011, Durand *et al.*, 2014, Ranzenbach *et al.*, 2013, Viola *et al.*, 2015). Nowadays, advanced computational resources have enhanced numerical simulation and have allowed to couple fluid and structural solvers to create Fluid-Structure Interaction simulations (Chapin *et al.*, 2011, Durand *et al.*, 2014, Ranzenbach *et al.*, 2013, Augier *et al.*, 2014, Lombardi *et al.*, 2012, Renzsch and Graf, 2010, Trimarchi *et al.*, 2013). However wind tunnel testing and full-scale testing are required for comparison and validation (Hansen *et al.*, 2002, Renzsch and Graf, 2013, Viola and Flay, 2011). Wind tunnel testing has the advantage to be in a controlled environment where a balance can be used to measure the forces created by the sails on the boat frame (Campbell, 2014a, Flay, 1996, Graf and Müller, 2009, Zasso *et al.*, 2005). Those results can easily be used to create a Velocity Prediction Program (Campbell, 2014b, Le Pelley and Richards, 2011). Nevertheless with wind tunnel testing, some rules of similitude are violated as the Reynolds number, or the ratio of fabric weight to wind

---

[1] julien.deparday@ecole-navale.fr

pressure or the ratio of membrane stress to wind pressure. Full-Scale testing does not have those issues, and permits to determine yacht performance in real sailing conditions. Those experiments need complex set-up in a harsh environment but actual aerodynamic loads can be assessed in a variety of ways. Sail boat dynamometers (Herman, 1989, Hochkirch and Brandt, 1999, Masuyama, 2014) measured forces from upwind sails transmitted to the boat frame. Fossati *et al.* (2015) created a sail boat dynamometer with the possibility of measuring aerodynamic forces of downwind sails. Augier *et al.* (2012) carried out experiments where loads on the rigging lines and sails were measured. They contributed to a better comprehension on interaction between the wind, the rigging and the sails. Le Pelley *et al.* (2015) measured the forces and the directions on the three corners of spinnakers. Le Pelley *et al.* (2012), Lozej *et al.* (2012), Motta *et al.* (2014), Viola and Flay (2010) measured pressures on sails for upwind and downwind sails.

However downwind sails are more complex to study than upwind sails mainly due to their non-developable 3D shape with highly cambered sections and massively detached flow around a thin and very flexible membrane. Due to the dynamic behavior of this unsteady fluid-structure interaction, the pressures on the sail vary quickly. Even in stable conditions, offwind sails have an inherent unsteadiness. One key feature of spinnaker unsteadiness comes from the flapping at the leading edge, also called luffing. We have previously investigated pressure evolution during luffing (Deparday *et al.*, 2014, Motta *et al.*, 2015). In Deparday *et al.* (2014), we showed an example where flapping of spinnaker creates pressure peaks at the leading edge increasing the aerodynamic force dynamically by 50%. Due to the non-stationarity of the environment while sailing, spatio-temporal pressure data are complex to analyze and therefore to simulate. However significant and different spatio-temporal patterns can be spotted (Motta *et al.*, 2015) and might be produced by different physical causes (Fluid-Structure Interaction, wind variations, boat motions, etc.). In this paper we present an approach to decompose complex pressure evolutions into simpler modes. It would then allow easier analysis and comparison with simulations.

This paper presents results of full-scale experiments of an instrumented J/80 class yacht in offwind conditions were loads, pressures on the spinnaker, boat and wind data were measured. After presenting the experimental apparatus, average and fluctuations of pressures and loads are presented. The next section is the use of the Proper Orthogonal Decomposition (POD) method on pressures to create a simpler model of the complex variations of pressure distribution in time. We show then that the method also helps to highlight the correlation between the main evolution of pressures and the variations of loads.

EXPERIMENTAL SETUP

An instrumented J/80 class sailing yacht, an 8 meter one-design cruiser racer was used during those experiments. A tri-radial asymmetrical spinnaker with a surface of about $65\,\mathrm{m}^2$ with a 12 meter long rounded luff was hoisted as well as a mainsail of $17\,\mathrm{m}^2$. Boat and wind data, loads on the standing rigging and on the sails were recorded. Moreover pressure taps, developed by the Yacht Research Unit from the University of Auckland were stuck on the spinnaker to acquire the dynamic pressure distribution. They were synchronized with the other data thanks to an acquisition software, RTMaps developed by Intempora which received every signal at their own rate and timestamped them "on the flow". A resampling was applied during the post processing to obtain synchronous data for easier analysis. Figure 1 shows the arrangement of all the sensors set onboard.

This setup for downwind navigation is a further development of the experimental system described in Augier *et al.* (2012) which was used for measurements in upwind navigation.
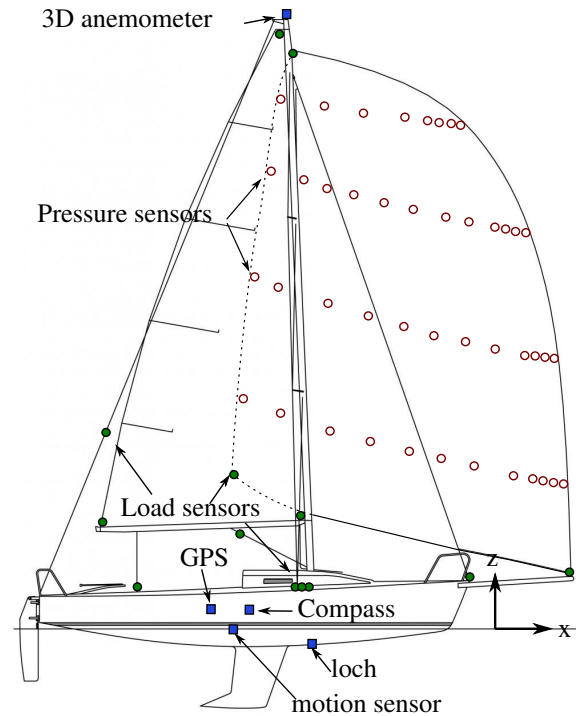

Figure 1: General arrangement of the experimental set-up on the J/80. 16 load sensors (green discs), 44 pressure taps (red circles), and wind and boat sensors (blue squares).

Loads

The standing rigging (shrouds, forestay and backstay) is fitted with custom-made turnbuckles and shackles equipped with strain gages. The running rigging (the corners of the

mainsail and of the spinnaker -head, tack and clew-) is equipped with instrumented shackles too. For the standing rigging and the mainsail the sensors are connected to a load acquisition system Spider8 from HBM. Voltages are received from all strain gages and amplified. They are then converted in digital data at a rate of 25 Hz. Thereafter they are transferred to the real-time acquisition software, RTMaps. Due to the high displacements of the spinnaker -in the order of magnitude of 1 to 5 meters for the spinnaker used in those experiments-, the instrumented shackles on the three corners of the spinnaker communicate wirelessly to the acquisition system. The clew sensor is connected via a wire running along the foot of the sail to a small box located near the tack point of the spinnaker (see Figure 2). This box contains two strain gage amplifiers, one for the tack sensor and one for the clew. A microcontroller receives and transmits data at a sampling frequency of 25 Hz to the receiver inside the boat via a wireless and low consumption ZigBee network. Another box is located at the head position for the head instrumented shackle. The delay between the emission and reception of data is insignificant compared to dynamics in sailing.

The errors of measurement are less than 2% of the measurement range (10 000 N for the shrouds, forestay and for the mainsail sheet, 5000 N for the backstay and other instrumented shackles on the mainsail and spinnaker).
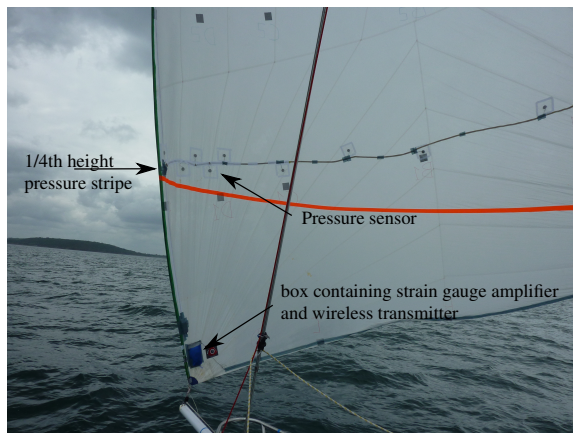

Figure 2: Photograph of the tack of the spinnaker used.

Pressures on spinnaker

On the spinnaker, 44 low range differential pressure sensors (Honeywell XSCL04DC) are located on the surface along 4 horizontal stripes: at 1/4, 1/2, 3/4 and 7/8th height of the spinnaker (see Figures 1 and 2). 12 transducers are used on each of the first 3 stripes and 8 for the top one. There is a higher concentration of pressure taps near the leading edge to be able to record potential leading edge suction peaks. Those sensors measure a difference of pressure between the extrados and intrados using the piezoresistive effect. There

is no need for a measure of a reference pressure, a complicated task in full-scale experiments. Those sensors are stuck on one side -at the intrados when sailing on portside tack- and are positioned facing 2mm-diameter holes on the sail to measure the pressure jump across the sail without significant air leak. Punctured light sail cloth patches are applied on the pressure taps to profile the sensors. This custom built pressure system was designed by the Yacht Research Unit at the University of Auckland. These pressure transducers are connected by wires to the receiver inside the boat and thus are synchronized with the other data.

The pressure sensors have a sampling frequency of approximatively 10 Hz with a maximum range of ± 1 kPa and a resolution of 0.5 Pa. The pressure acquisition system is more described in Motta *et al.* (2014).

Procedure

Sea trials were performed in the bay of Brest, France, offshore Ecole Navale. During those experiments the weather conditions were stable:

- average true wind speed: 6 m/s (12 kn)
- gust: 8 m/s (16 kn)
- wind direction: 270° (westerly wind). Stable. Flat water.

Even in conditions considered as "stable" (with no gust, no wind shift, on flat water and fixed trimming), offwind sails have an inherent unsteadiness, like luffing (flapping at the leading edge). To keep "stable" conditions, a standard procedure must be followed. During those experiments, the controlled inputs were the apparent wind angle and the trim of the spinnaker. Trimmer and helmsman were kept the same for the whole test. The trimmer adjusted the spinnaker at the optimum trim (i.e. on the verge of luffing at the leading edge). The helmsman kept the apparent wind angle as constant as possible.

During the post-processing routine, periods of 5 seconds minimum were labelled "stable" when the standard deviation of the apparent wind angle (AWA) was below 4° and the standard deviation of the apparent wind speed (AWS) was below 10% of the average. Those periods were extended in time as long as those criteria were met. A large range of AWA (between 55° and 140°) is swept by the "stable" periods found, with a certain redundancy for most of the AWA. Each stable period is processed individually.

AVERAGES AND FLUCTUATIONS

Pressures

The average pressure distribution and loads are compared according to the apparent wind angle. A large range of apparent wind angles (AWA) has been met in a rather constant true wind speed (TWS) between 5.8 m/s and 7.1 m/s thus between 11.2 kn to 13.8 kn. The apparent wind angle is mea-
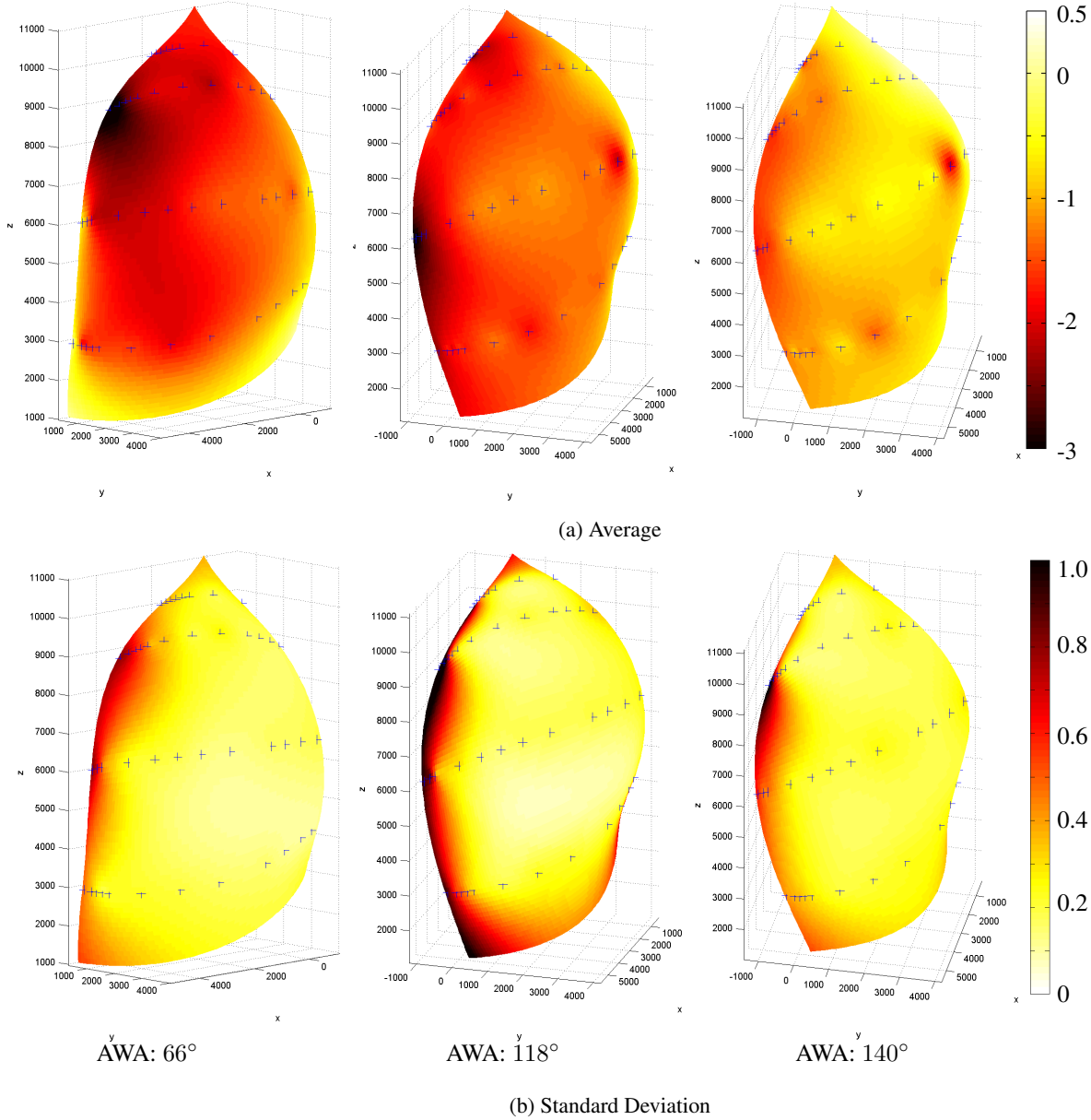
(a) Average

AWA: 66°   AWA: 118°   AWA: 140°

(b) Standard Deviation

Figure 3: Pressure distributions, time average pressure coefficient ΔC_P (a) and the fluctuations (b) for 3 typical AWA ($66°$, $118°$, $140°$). Blue crosses show the positions of the pressure taps.

sured at the mast head. One should be aware this measure is affected by the twist of the wind, the upwash effect from the sails and the heel.

To display the pressure distribution on the whole sail from discrete measurement points, a linear Radial Basis Function interpolation has been used. On following figures where the pressure distribution is displayed on the spinnaker, blue crosses show where the pressure measurement sensors were located on the sail. Thus pressures at those blue crosses are actual measured values, when the pressure distribution is interpolated between the stripes and pressure taps. With no information on the sail boundaries, values at the top (above 7/8th) and at the bottom (below 1/4th) are extrap-

olated. The shapes used to display the pressure distributions come from other experiments with the same spinnaker where photogrammetric measurements were carried out to acquire the flying shapes.

Time-Averaged pressure distributions for similar apparent wind angles have good repeatability. Moreover the pressure distribution evolves clearly with the AWA. Figure 3a presents 3 characteristic pressure spatial distributions at $66°$, $118°$ and $140°$. It shows the coefficient of the difference of pressure as commonly defined in aerodynamics:

$$\Delta C_P = \frac{P_{\text{leeward}} - P_{\text{windward}}}{\frac{1}{2}\rho(\text{AWS})^2}.$$

At tight angles as AWA 66°, a bulb of high suction is found at the leading edge in the top half of the spinnaker ($\Delta C_P \approx -3$) which produces high aerodynamic force. ΔC_P on the rest of the sail is around -2 increasing to -1/-0.5 at the trailing edge.

At AWA around 110°-120°, the area where the peak of suction occurs is smaller around half of the spinnaker height and the absolute value lower. On the rest of the spinnaker, the pressure coefficient on the spinnaker is rather constant around -1.2 and increasing to -0.5 at the trailing edge.

At AWA 140°, the decrease of suction is even more visible on the whole sail with almost no suction peak at the leading edge and with a reduction of $|\Delta C_P|$ along the flow up to a positive ΔC_P at the trailing edge even on the actual measured points. Positive pressure coefficient means a collapse of the sail at the trailing edge and thus an unstable flying shape. It is consistent with what the authors have noticed during experiments: at large AWA, the spinnaker starts collapsing first at the leech and not at the luff.

While the AWA is increased, not only is a clear decrease of absolute differential pressure coefficient (from -3 down to 0 about), but also the AWS decreases (from 7 m/s to 3.5 m/s about). So the absolute values of ΔP decrease even more dramatically: At tight AWA, around 65°, the order of magnitude of differential pressure is -40 Pa, and only -4 Pa at large AWA –around 140°-.

Figure 3b shows the standard deviation for the corresponding AWA. Standard deviation on the whole sail is interpolated from the standard deviations calculated on the pressure taps only. Higher standard deviations mean bigger variations of pressure during a "stable" period. Despite a clear difference for the pressure distribution on the whole spinnaker depending on the AWA, pressure variations during the "stable" periods have similar spatial patterns. Strong variations are found at the leading edge, around 1, on the whole height for 66° and 118° while the rest of the spinnaker has a standard deviation of about 0.2. However, while the order of magnitude of standard deviation of ΔC_P is similar for every AWA, the relative variation of pressures compared with the average pressure coefficient varies. Variations are more significant for large AWA (around 120°-140°) than for tight AWA. For tight AWA, the standard deviation is around 30 Pa thus 75% of the average pressure. For large AWA, the standard deviation is around 8 Pa thus 2 times bigger than the average pressure.
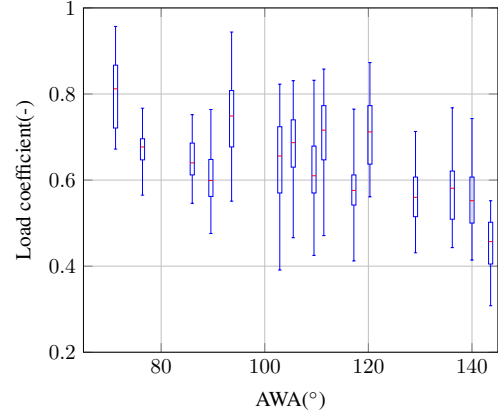
Loads

Figure 4 displays the load coefficients on the three corners of the spinnaker according to the apparent wind angle:
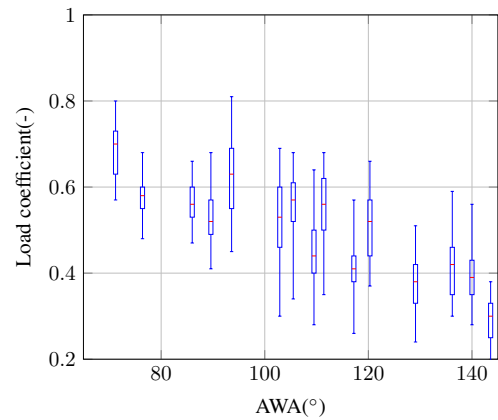
$$C_F = \frac{\text{Load}}{\frac{1}{2}\rho \, \text{S(AWS)}^2}$$

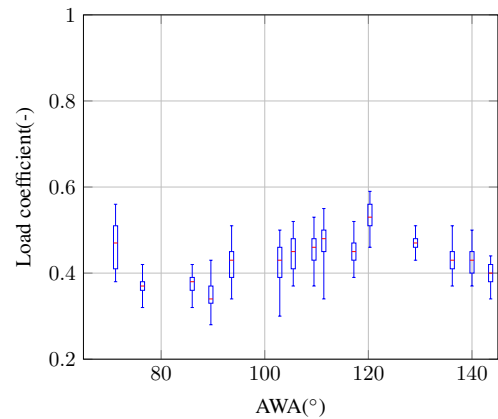with S the sail area of the spinnaker.
In Figure 4, only "stable" periods of 10 seconds minimum

(a) Head coefficient

(b) Tack coefficient

(c) Clew coefficient

Figure 4: Boxplot for load coefficients C_F at the three corners of the spinnaker for different AWA. Central red mark is the median, the box represent the interquartile range between the lower and upper quartiles. It contains 50% of the loads. The upper and lower whiskers indicate the minimum and maximum values.

are taken. Even though the periods chosen are "stable", loads can vary significantly. Therefore each period for a

specific average apparent wind angle is displayed as a box plot. The central red mark is the median, and the edges of the box are the lower and upper quartile. The lower quartile (Q1) splits off the lowest 25% of data from the highest 75%. The upper quartile (Q3) splits off the highest 25% of loads from the lowest 75%. The box represents the interquartile range (IQR = Q3 –Q1). It contains 50% of the loads recorded during one "stable" period. The whiskers show the maximum and minimum loads recorded.

Figure 4 shows also the general trend of the load co-efficients on the three corners according to the apparent wind angle. Head and tack have similar evolution with a decrease especially between $110°$ and $140°$ respectively from 0.8 to 0.5 and from 0.7 to 0.3. Whereas clew load coefficient is approximatively constant around 0.4.

As explained previously, when the AWA is increased, the AWS decreases. While at clew point, the absolute loads decrease only due to the decrease of the AWS, at tack and head points the absolute loads decrease even more significantly.

Q3 can be seen as an arbitrary separation between the small variations of loads around the median (inside the IQR) and the peaks of loads (in the top quarter). The IQR has the same relative range for every AWA, between –10% and +10% of the median for the most loaded corners (head and tack) and between -5% and +5% for the clew. Since the IQR is relatively constant and small, one can conclude that for every AWA, without taking into account peaks of loads, the averaged load coefficient is rather stable and varies slightly.

For the most loaded corners (head and tack) the upper whisker (maximum load) is about 20% higher than the median for tight angles (AWA $<$ $100°$) and 30% for large angles (AWA $>$ $120°$). For the clew point the upper whisker is always about 15% higher than the median for all AWA. Relative variations of loads seem fairly constant for every AWA, and slightly bigger for large AWA at the head and tack points.

It is interesting to note that most variations of loads are present at the head and tack points, the closest points of the leading edge where the highest variations of pressure occur. While at clew point, the relative variation of loads is smaller.

Those variations of loads and pressures are unsteady even during "stable" periods. However specific patterns might be spotted and might be linked to different causes. The yacht motion and its influence on the apparent wind (pitching and rolling of the boat), gusts (pure aerodynamic cause), vortex shedding, or a change of the spinnaker shape as luffing (unsteady fluid-structure interaction) could make the spinnaker forces vary.

Therefore, we would like to extract patterns in order to decompose complex pressure evolutions into simpler modes. Those pressure modes could help to describe a tem-poral global behavior in a better way than analyzing each pressure sensor signal, and could be correlated with other recorded data. We decided to use the Proper Orthogonal Decomposition method to characterize the spatial pattern of pressure variations.

DECOMPOSITION INTO MODES

Proper Orthogonal Decomposition method

The Proper Orthogonal Decomposition (POD), is based on the Karhunen-Loeve expansion and also called Principal Component Analysis, PCA. It was first introduced in the context of Fluid Mechanics by (Lumley, 1967). The input data (in our case $\Delta C_P(x,t)$) can be expanded into orthog-onal basis functions $\phi_i(x)$ with time coefficient $a_n(t)$:

$$U(x,t) = \sum_n a_n(t) \cdot \phi_n(x).$$

As proper modes are derived from the data itself (data driven decomposition), there is no need of a-priori knowl-edge or education scheme. Moreover, each basis function has its own amount of fluctuation energy different from each other. These functions are statistically optimal in the least mean-square sense. As a result, fluctuation energy drops down quickly which means a low number of modes is needed in the expansion to reproduce the main variations of the field. POD is a powerful tool for generating lower dimensional models of dynamical systems.

Most of the time, POD is used on the fluctuations of the input data only. After subtracting the average compo-nent (seen as the zeroth mode) from the data, a matrix U is created as a set of N observations (commonly called snap-shots) of M records. Each column contains all fluctuating input data (M values) from a specific snapshot and each row contains all snapshots (N snapshots) from a specific measurement point.

$$\mathbf{U} = \begin{bmatrix} u_{11} & u_{12} & \cdots & u_{1N} \\ u_{21} & u_{22} & \cdots & u_{2N} \\ \vdots & \ddots & \ddots & \vdots \\ u_{M1} & u_{M2} & \cdots & u_{MN} \end{bmatrix}$$

Then the auto covariance matrix C (MxM) is calculated as:

$$\mathbf{C} = \mathbf{U} * \mathbf{U}^T$$

because $M >> N$. We have M= 44 measurement points and $N \approx 20000$. However in fluid mechanics, it is com-mon to have $N >> M$ when using PIV or CFD results for example. For those cases the so-called "Snapshot POD" introduced first by (Sirovich, 1987) is used. For our ex-periments, the "Direct POD" has been applied. The corre-sponding eigenvalue problem of the auto covariance matrix is solved:

$$\mathbf{C} * \mathbf{\Phi} = \lambda * \mathbf{\Phi}$$

The eigenvectors $\Phi(i)$ are the POD modes. POD modes are sorted in descending order according to their corresponding eigenvalue $\lambda(i)$ which represent their energy. The POD mode with the highest corresponding eigenvalue is mode 1. The expansion coefficient (or mode time coefficient) is calculated as follows:

$$\mathbf{a} = \mathbf{U}^T * \mathbf{\Phi}$$

POD results

Following results presented here are for a "stable" period with an average AWA of $69°$, but is representative to what we have observed for different periods at different AWA. This point will be discussed further in the article. Figure 5 shows the energy distribution for each POD mode. The first mode contains almost 45% of the fluctuation energy. Mode 2 and 3 represent only 15% each. And most of the time other modes have less than 5% of the fluctuation energy. It is clear that the first mode is dominant compared to the others.

The pressure distribution evolution can be simplified by taking only the first terms of the expansion. The reconstruction using the first modes allows to only keeping the most energetic part of the signal and removing insignificant variations and noises. The precision of the reconstruction has been calculated according to the number of modes. With mode 0 (the average) and mode 1, 85% of the signal is already reconstructed. With 3 modes, the error of reconstruction of the pressure signals is 10%. About 10 modes are required to achieve a reconstruction with less than 5% of difference.
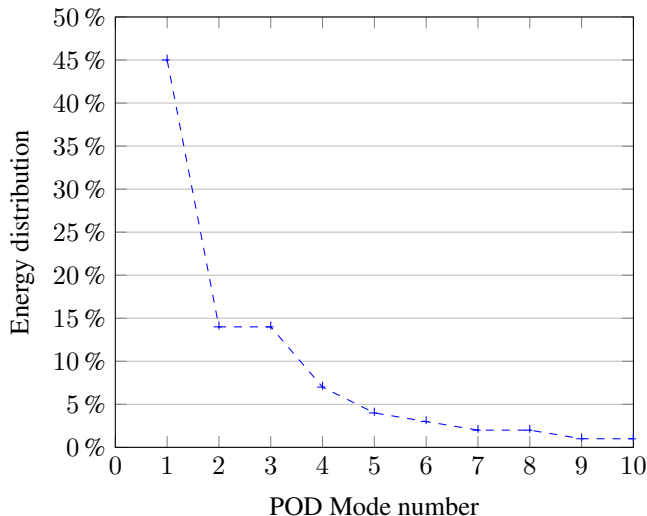

Figure 5: Energy distribution of the fluctuations for the first 10 modes for AWA $69°$.

Figure 6 presents the first 3 modes. The scale value is arbitrary. To represent a fluctuation of Cp, they must be multiplied by the corresponding mode time coefficient depending on the time - which can be positive or negative - (presented in Figure 8). Mode 1 has a bulb of pressure on the top half of the spinnaker at the leading edge and a smaller bulb of opposite sign on the bottom half height of the spinnaker. Mode 2 is similar with the standard deviation pattern presented before. Mode 3 and further modes display smaller coherent patterns and may change with the period used.

Table 1 shows the energy distribution for different "stable" periods at different AWA. The ratio of energy of each mode number is rather constant for every AWA. Moreover each mode number has a similar pattern of pressure distribution, even though it happens that mode 2 and mode 3 are inverted in a few cases.

To compare modes, the maximum value of time coefficient is taken to be multiplied by the spatial mode: $\max(a_1(t)) \cdot \phi_1(x)$. Maximum value of time coefficient is used since we want to analyze and compare dominant variations. Moreover, by mathematical definition: $\forall n, \overline{a_n(t)} = 0$ and thus is irrelevant to be used for comparison. Maximum values of mode 1 for different AWA are presented in Figure 7 at 4 different stripes where the pressures are measured (1/4, 1/2, 3/4, 7/8th height of the spinnaker). Differential pressure coefficients have comparable shapes for every AWA, except that $|\Delta C_P|$ on the bottom half is slightly smaller for deeper AWA. The bulb of suction at the leading edge at 7/8 and 3/4 of the spinnaker height is always present and a smaller bulb of positive ΔC_P at 1/2 and 1/4 height is also spotted. Even if the POD method is a data driven decomposition (i.e. modes are derived from the data itself), there is a good repeatability of POD modes for "stable" periods when the spinnaker has a fixed trim. Moreover mode 1, which plays an important role in the fluctuation of pressures, could be defined as a unique mode whatever the AWA.

Table 1: Energy distribution of the fluctuations for the first 10 modes for different AWA.

Modes	66 deg	98 deg	120 deg	140 deg
1	43%	46%	45%	45%
2	21%	16%	19%	15%
3	8%	9%	10%	11%
4	7%	6%	6%	7%
5	4%	5%	3%	5%
6	3%	4%	3%	3%
7	2%	3%	2%	2%
8	2%	2%	2%	2%
9	2%	2%	2%	2%
10	1%	1%	1%	1%

POD modes evolve in time. When the time coefficient of a corresponding mode is at an extremum, the corresponding mode is then preponderant. Analyzing time coefficients would then help to link pressure variations with other recorded data.

Figure 8 shows the evolution of the time coefficient for the first 3 modes. Amplitudes of mode 1 are bigger than the
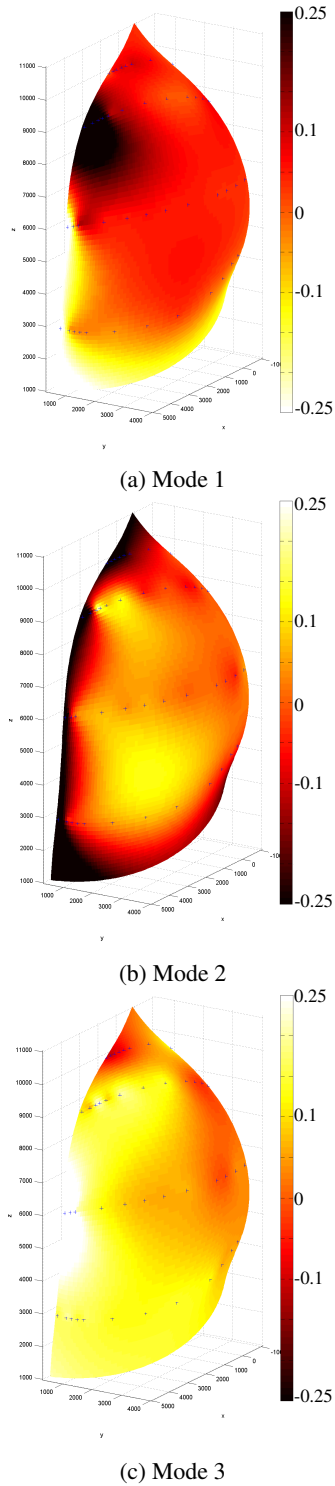
(a) Mode 1

(b) Mode 2

(c) Mode 3

Figure 6: First 3 spatial orthogonal modes from POD method for AWA $69°$. Mode 1 is the most energetic mode.

Figure 7: Mode 1 for maximum time coefficient $max(a_1(t) \cdot \phi_1(x))$ for different AWA.

other modes as expected due to the larger energy it possesses. Mode 1 and mode 2 are slightly correlated; mode 2 is shifted of a quarter of a pseudo-period. It means when mode 1 is maximal, mode 2 is null. A typical pseudo period for mode 1 stands out for this AWA $69°$. Furthermore,
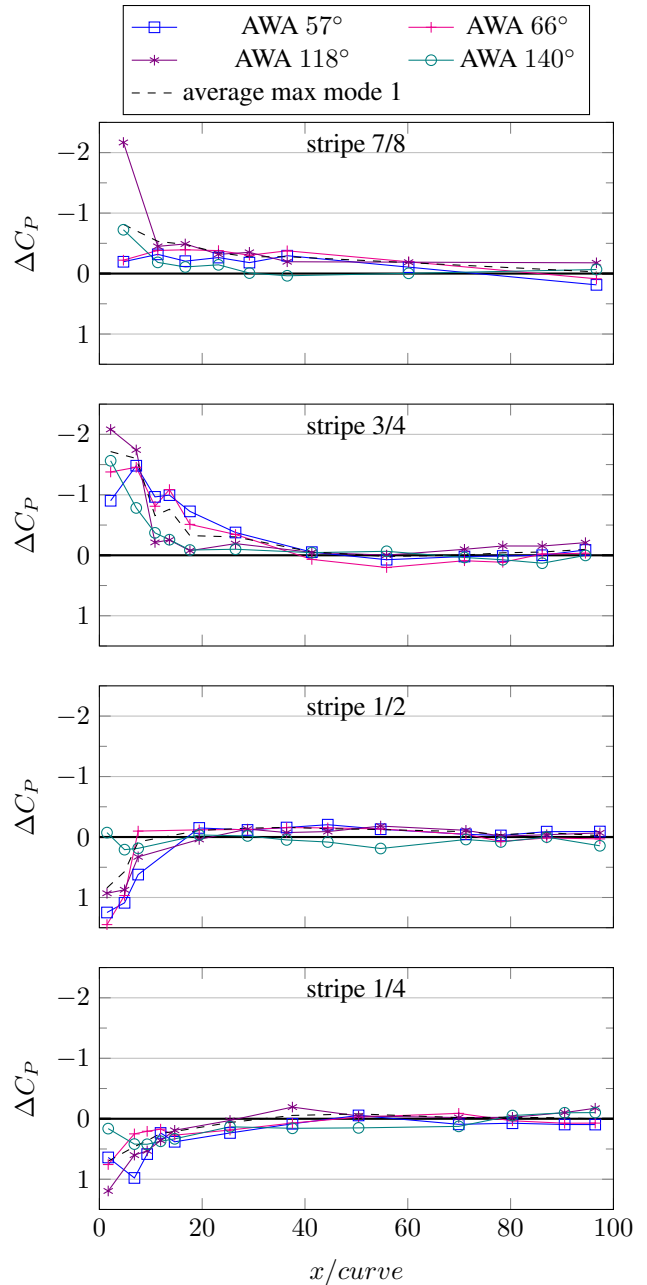
for different "stable" periods, at different AWA -not displayed here-, similar variations of the temporal coefficient of mode 1 are detected. However the dynamics change with the AWA. The pseudo-period is measured, and the corresponding frequency is displayed in Table 2 with the corresponding average AWS of the "stable" period. The reduced frequency is calculated as follows:

$$f_r = \frac{f_s \cdot \sqrt{S}}{AWS}$$

with S the sail area, thus $\sqrt{S} = 8.3\,\text{m}$.

When the AWA is increased, the typical pseudo frequency of the time coefficient of mode 1 is reduced by a factor of 2.5. The AWS decreases at a similar rate. A ratio of 2.1 is found between AWA $57°$ and $140°$. Therefore the reduced frequency is nearly constant with a small decrease. The dependence of the pseudo-frequency with the AWS might demonstrate that mode 1 is mostly driven by aerodynamic phenomena as expected, and not by mechanical resonance of the rigging or of the membrane of the sail.

In conclusion, the spatial pattern of mode 1 does not change with the AWA, but only the temporal dynamics with an increase of the pseudo-period when the AWA increases.
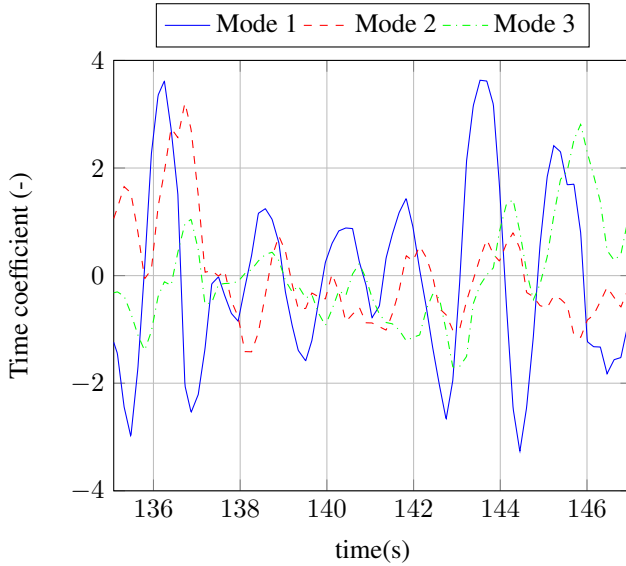

Figure 8: Time coefficient $a_n(t)$ for the first three modes for AWA $69°$.

Table 2: Pseudo-frequency and reduced frequency for different AWA.

AWA($°$)	f_s(Hz)	AWS(m/s)	f_r(-)
57	1.5	7.0	1.78
66	1.3	6.4	1.69
69	1.3	6.2	1.73
98	1	5.4	1.53
118	0.7	3.7	1.57
140	0.6	3.3	1.52

Table 3 presents the cross-correlation of all data measured for the specific period presented in (Deparday *et al.*, 2014) where loads and flapping were strongly correlated. The normalized cross-correlation is calculated with the time coefficients of the first three modes. Cross correlation between two signals X and Y is defined as follow:

$$C_{xy}(\tau) = \mathcal{E}[(X(t_2) - \mu_{X(t_2)}) - (Y(t_1) - \mu_{Y(t_1)})]$$

where $\mathcal{E}[\cdot]$ is the expected value operator, $\tau = t_2 - t_1$ is the shift applied between two signals. μ_X and μ_{UY} are the mean functions.

The cross correlation matrix is calculated to determine the correlations of every signal with each other. The values are between 0 (not correlated at all) and 1 (same dynamics of the signal). The diagonal represents the auto-correlation of every signal.

A very strong correlation is present between the loads except with the forestay and the shroud D1 leeward as they are not loaded and slack. Loads are also slightly correlated with the yaw. The shift between the two signals is about 1 second in advance for the loads. A peak of aerodynamic loads might modify the aerodynamic center of effort and thus change the equilibrium of the sailing yacht and make the course vary.

The time coefficient of mode 1 is also well correlated with the loads (around 0.9). There is no delay between mode 1 and the spinnaker aerodynamic loads. Spinnaker aerodynamic loads are $0.1\,\text{s}$ in advance of the standing rigging loads. In this case the pressure evolution is instantaneously transmitted to the corners of the spinnaker which then transmit this increase of loads to the shrouds and backstay. Mode 1 is a good parameter to define peaks of loads due to flapping of the spinnaker.

Here mode 2 is reasonably correlated with mode 1 with a coefficient of 0.72. The shift between the two modes is $0.4\,\text{s}$. As explained previously with Figure 8, mode 2 is shifted of a quarter of a pseudo-period. Thus the pseudo-frequency for this specific period should be around $T = 4 \cdot 0.4\,\text{s} = 1.6\,\text{s}$. This pseudo-period corresponds to what was presented in Deparday *et al.* (2014).

In conclusion, mode 1 describes well the flapping of the luff. It can be represented as a unique spatial pattern for every AWA and thus is a good indicator of the dynamics of the spinnaker. Its temporal pseudo-period slows down as the AWS decreases when the AWA is increased.

Table 3: Cross-correlation between different signals recorded during experiments, and mode 1, 2 and 3 of the POD.

	forestay	backstay	V1 windw'd	D1 windw'd	D1 leew'd	Head	Tack	Clew	mode 1	mode 2	mode 3	roll	pitch	yaw	AWA	AWS	BS
forestay	1.00	0.58	0.62	0.63	0.78	0.59	0.59	0.59	0.65	0.62	0.59	0.60	0.69	0.51	0.73	0.59	0.40
backstay	0.58	1.00	0.88	0.92	0.62	0.96	0.95	0.93	0.91	0.66	0.45	0.58	0.61	0.75	0.58	0.49	0.57
V1 windw'd	0.62	0.88	1.00	0.99	0.79	0.94	0.94	0.94	0.85	0.66	0.41	0.48	0.61	0.68	0.63	0.50	0.44
D1 windw'd	0.63	0.92	0.99	1.00	0.79	0.95	0.95	0.95	0.88	0.68	0.41	0.54	0.61	0.71	0.63	0.54	0.46
D1 leew'd	0.78	0.62	0.79	0.79	1.00	0.69	0.70	0.76	0.66	0.53	0.52	0.49	0.52	0.65	0.60	0.54	0.44
Head	0.59	0.96	0.94	0.95	0.69	1.00	1.00	0.98	0.90	0.63	0.47	0.58	0.57	0.71	0.63	0.53	0.57
Tack	0.59	0.95	0.94	0.95	0.70	1.00	1.00	0.98	0.88	0.61	0.45	0.54	0.55	0.71	0.62	0.51	0.58
Clew	0.59	0.93	0.94	0.95	0.76	0.98	0.98	1.00	0.85	0.65	0.44	0.63	0.58	0.70	0.67	0.61	0.60
mode 1	0.65	0.91	0.85	0.88	0.66	0.90	0.88	0.85	1.00	0.72	0.43	0.52	0.63	0.74	0.54	0.47	0.38
mode 2	0.62	0.66	0.66	0.68	0.53	0.63	0.61	0.65	0.72	1.00	0.46	0.64	0.84	0.60	0.68	0.48	0.29
mode 3	0.59	0.45	0.41	0.41	0.52	0.47	0.45	0.44	0.43	0.46	1.00	0.66	0.41	0.45	0.56	0.75	0.51
roll	0.60	0.58	0.48	0.54	0.49	0.58	0.54	0.63	0.52	0.64	0.66	1.00	0.83	0.83	0.77	0.88	0.47
pitch	0.69	0.61	0.61	0.61	0.52	0.57	0.55	0.58	0.63	0.84	0.41	0.83	1.00	0.76	0.85	0.68	0.28
yaw	0.51	0.75	0.68	0.71	0.65	0.71	0.71	0.70	0.74	0.60	0.45	0.83	0.76	1.00	0.66	0.56	0.46
AWA	0.73	0.58	0.63	0.63	0.60	0.63	0.62	0.67	0.54	0.68	0.56	0.77	0.85	0.66	1.00	0.58	0.52
AWS	0.59	0.49	0.50	0.54	0.54	0.53	0.51	0.61	0.47	0.48	0.75	0.88	0.68	0.56	0.58	1.00	0.50
BS	0.40	0.57	0.44	0.46	0.44	0.57	0.58	0.60	0.38	0.29	0.51	0.47	0.28	0.46	0.52	0.50	1.00

CONCLUSIONS

Full-Scale experiments were carried out on an instrumented J/80 sailing yacht where loads, pressure distribution on the spinnaker boat and wind data were measured at different downwind angles.

We show pressure coefficients and load coefficients decrease when the AWA is increased, whereas variations of load and pressure coefficients are mainly constant. Therefore variations relative to the average loads or pressures are bigger for larger AWA. Moreover we found that most of the pressure and load variations are mainly at the luff for every AWA.

A POD analysis has been used on pressure signals in order to identify the most energetic patterns. The first mode of the POD method is uniquely identified for every AWA, and is well associated with the flapping of the luff producing correlated variations of loads on the 3 corners of the spinnaker. It has a unique spatial mode of pressure fluctuations for all AWA. Only the temporal behavior differs with the AWA. An identified typical pseudo-period of flapping has been calculated thanks to this first mode. It shows a linear decrease of the pseudo-frequency with the AWS. Flapping of the luff might be the result of an aerodynamic phenomenon.

Moreover POD enables to characterize a global unsteady behavior instead of analyzing all local pressure time series

This paper presented a way to characterize the pressure evolution due to flapping. It permits to show to sail designers where the highest variations of pressure occur when flapping. Moreover thanks to the POD method, the first modes allow to reconstruct a signal with the main variations (i.e. with the most energetic part) and remove noises. Therefore comparison with other measurements or numerical simulations is simplified.

ACKNOWLEDGEMENTS

References

CHAPIN, V.G., DE CARLAN, N. and HEPPEL, P., *A Multidisciplinary Computational Framework for Sailing Yacht Rig Design & Optimization through Viscous FSI*, 20th Chesapeake Sailing Yacht Symposium, March, (1–17), Annapolis (2011).

DURAND, M., LEROYER, A., LOTHODÉ, C., HAUVILLE,

F., VISONNEAU, M., FLOCH, R. and GUILLAUME, L., *FSI investigation on stability of downwind sails with an automatic dynamic trimming*, Ocean Engineering, **90**, (2014), 129–139.

RANZENBACH, R., ARMITAGE, D. and CARRAU, A., *Mainsail Planform Optimization for IRC 52 Using Fluid Structure Interaction*, 21st Chesapeake Sailing Yacht Symposium, March, (50–58), Annapolis (2013).

VIOLA, I.M., BIANCOLINI, M.E., SACHER, M. and CELLA, U., *A CFD-based wing sail optimisation method coupled to a VPP*, 5th High Performance Yacht Design Conference, (1–7), Auckland (2015).

AUGIER, B., HAUVILLE, F., BOT, P., AUBIN, N. and DU-RAND, M., *Numerical study of a flexible sail plan submitted to pitching: Hysteresis phenomenon and effect of rig adjustments*, Ocean Engineering, **90**, (2014), 119–128.

LOMBARDI, M., CREMONESI, M., GIAMPIERI, A. and PAROLINI, N., *A strongly coupled fluid-structure inter-action model for wind-sail simulation*, 4th High Performance Yacht Design Conference, (212–221), Auckland (2012).

RENZSCH, H. and GRAF, K., *Fluid Structure Interaction Simulation of Spinnakers–Towards Simulation Driven Sail Design*, 21st HISWA Symposium on Yacht Design and Yacht Construction (2010).

TRIMARCHI, D., VIDRASCU, M., TAUNTON, D., TURNOCK, S. and CHAPELLE, D., *Wrinkle development analysis in thin sail-like structures using MITC shell finite elements*, Finite Elements in Analysis and Design, **64**, (2013), 48–64.

HANSEN, H., JACKSON, P. and HOCHKIRCH, K., *Comparison of Wind Tunnel and Full-Scale Aerodynamic Sail Force measurements*, High Performance Yacht Design Conference, Auckland (2002).

RENZSCH, H. and GRAF, K., *An experimental validation case for fluid-structure-interaction simulations of downwind sails*, 21st Chesapeake Sailing Yacht Symposium, March, (59–66), Annapolis (2013).

VIOLA, I.M. and FLAY, R.G., *Sail pressures from full-scale, wind-tunnel and numerical investigations*, Ocean Engineering, **38**(16), (2011), 1733–1743.

CAMPBELL, I.M.C., *A comparison of downwind sail coefficients from tests in different wind tunnels*, Ocean Engineering, **90**, (2014a), 62–71.

FLAY, R.G., *A twisted flow wind tunnel for testing yacht sails*, Journal of Wind Engineering and Industrial Aero-dynamics, **63**(1-3), (1996), 171–182.

GRAF, K. and MÜLLER, O., *Photogrammetric Investigation of the Flying Shape of Spinnakers in a Twisted Flow Wind Tunnel*, 19th Cheasapeake Sailing yacht Symposium, March, Annapolis (2009).

ZASSO, A., FOSSATI, F. and VIOLA, I.M., *Twisted Flow Wind Tunnel Design for Yacht Aerodynamic Studies*, EACWE4 - The 4th European & African Conference on Wind Engineering, (1–14), Prague (2005).

CAMPBELL, I.M.C., *Comparison of downwind sailing performance predicted from wind tunnel tests with full-scale trials from America's Cup class yachts*, 23rd HISWA Symposium on Yacht Design and Yacht Construction (2014b).

LE PELLEY, D. and RICHARDS, P., *Effective Wind Tunnel Tesing of Yacht Sails Using a Real-Time Velocity Prediction Program*, 20th Cheasapeake Sailing Yacht Symposium, Annapolis (2011).

HERMAN, J.S., *A sail force dynamometer: design, implementation and data handling*, Ph.D. thesis, Massachussets Institute of Technology (1989).

HOCHKIRCH, K. and BRANDT, H., *Fullscale hydrodynamic force measurement on the Berlin sailing dynamometer*, 14th Chesapeake Sailing Yacht Symposium, (33–44), Annapolis (1999).

MASUYAMA, Y., *The work achieved with the sail dynamometer boat "Fujin", and the role of full scale tests as the bridge between model tests and CFD*, Ocean Engineering, **90**, (2014), 72–83.

FOSSATI, F., BAYATI, I., ORLANDINI, F., MUG-GIASCA, S., VANDONE, A., MAINETTI, G., SALA, R., BERTORELLO, C. and BEGOVIC, E., *A novel full scale laboratory for yacht engineering research*, Ocean Engineering, **104**, (2015), 219–237.

AUGIER, B., BOT, P., HAUVILLE, F. and DURAND, M., *Experimental validation of unsteady models for fluid structure interaction: Application to yacht sails and rigs*, Journal of Wind Engineering and Industrial Aerodynamics, **101**, (2012), 53–66.

LE PELLEY, D.J., RICHARDS, P.J. and BERTHIER, A., *Development of a directional load cell to measure flying sail aerodynamic loads*, 5th High Performance Yacht Design Conference, (66–75), Auckland (2015).

LE PELLEY, D., MORRIS, D. and RICHARDS, P., *Aerodynamic force deduction on yacht sails using pressure and shape measurements in real time*, 4th High Performance Yacht Design Conference, (28–37), Auckland (2012).

LOZEJ, M., GOLOB, D. and BOKAL, D., *Pressure distribution on sail surfaces in real sailing conditions*, 4th High Performance Yacht Design Conference, (242–251), Auckland (2012).

MOTTA, D., FLAY, R.G., RICHARDS, P.J., LE PELLEY, D.J., DEPARDAY, J. and BOT, P., *Experimental investigation of asymmetric spinnaker aerodynamics using pressure and sail shape measurements*, Ocean Engineering, **90**, (2014), 104–118.

VIOLA, I.M. and FLAY, R.G., *On-water pressure measurements on a modern asymmetric spinnaker*, 21st HISWA Symposium on Yacht Design and Yacht Construction, November, Amsterdam (2010).

DEPARDAY, J., BOT, P., HAUVILLE, F., MOTTA, D., LE PELLEY, D.J. and FLAY, R.G.J., *Dynamic measurements of pressures, sail shape and forces on a full-scale spinnaker*, 23rd HISWA Symposium on Yacht Design and Yacht Construction, Amsterdam (2014).

MOTTA, D., FLAY, R., RICHARDS, P., PELLEY, D.L., BOT, P. and DEPARDAY, J., *An investigation of the dynamic behaviour of asymmetric spinnakers at full-scale*, 5th High Performance Yacht Design Conference, (76–85), Auckland (2015).

LUMLEY, J., *The structure of inhomogeneous turbulence*, A. Yaglom and V. Tatarski, eds., Atmospheric Turbulence and Wave Propagation, (166–178), Nauka, Moscow (1967).

SIROVICH, L., *Turbulence and the dynamics of coherent structures part i: coherent structures*, Quarterly of Applied Mathematics, **XLV**(3), (1987), 561–571.